Research Square

Preprints are preliminary reports that have not undergone peer review.
They should not be considered conclusive, used to inform clinical practice,
or referenced by the media as validated information.

An intracellular auxin rheostat fine-tunes growth and wood patterning in poplar

Daniel Conde

daniel.conde@upm.es

Centro de Biotecnología y Genómica de Plantas https://orcid.org/0000-0001-8362-4190

Juan Murillo Murillo

Centro de Biotecnología y Genómica de Plantas https://orcid.org/0009-0008-4581-8224

Miguel Rodrigo

Centro de Biotecnología y Genómica de Plantas https://orcid.org/0009-0003-5304-8331

Alejandro Díaz

Universidad Politécnica de Madrid

Paolo Triozzi

https://orcid.org/0000-0003-0192-3336

Isabel Allona

Centre for Plant Biotechnology and Genomics UPM, Spain https://orcid.org/0000-0002-7012-2850

Mariano Perales

Centre for Plant Biotechnology and Genomics UPM, Spain https://orcid.org/0000-0002-7351-8439

Krzysztof Wabnik

Centro de Biotecnologıa y Genomica de Plantas (Universidad Politecnica de Madrid - Instituto Nacional de Investigacion y Tecnologıa Agraria y Alimentaria) https://orcid.org/0000-0001-7263-0560

Article

Keywords:

Posted Date: September 4th, 2026

DOI: https://doi.org/10.21203/rs.3.rs-10386641/v1

License: This work is licensed under a Creative Commons Attribution 4.0 International License.
Read Full License

Additional Declarations: There is **NO** Competing Interest.

Title: An intracellular auxin rheostat fine-tunes growth and wood patterning in poplar

Authors:

Juan Murillo[1,†], Miguel Rodrigo[1,†], Alejandro Piedrabuena-Díaz[1], Paolo M Triozzi[2], Isabel Allona[1,3], Mariano Perales[1,3], Krzysztof Wabnik[1,3*], Daniel Conde[1,*]

Affiliations:

[1] Centro de Biotecnología y Genómica de Plantas, Universidad Politécnica de Madrid - Instituto Nacional de Investigación y Tecnología Agraria y Alimentaria (INIA-CSIC), Madrid, 28223, Spain.

[2] Institute of Plant Sciences, Sant'Anna School of Advanced Studies, Pisa, 56010, Italy

[3] Departamento de Biotecnología-Biología Vegetal, Escuela Técnica Superior de Ingeniería Agronómica, Alimentaria y de Biosistemas, Universidad Politécnica de Madrid, Madrid, 28040, Spain.

[†] Co-first author

[*] Corresponding authors:

Daniel Conde: daniel.conde@upm.es; Krzysztof Wabnik: k.wabnik@upm.es

ABSTRACT

Wood formation and tree growth depend on the precise spatiotemporal distribution of auxin, yet how woody perennials dynamically regulate local auxin pools remains poorly understood. Here, we demonstrate that the tonoplast-localized transporters WAT1 and WAT2 drive cambial activity, secondary growth, and wood patterning in poplar by controlling stem free auxin availability. Unlike annual models such as *Arabidopsis*, simultaneous disruption of WAT1 and WAT2 in poplar induces severe dwarfism and marked wood defects, yielding smaller, denser vessel elements, all of which were rescued by genetic complementation. Loss of WAT function depleted stem indole-3-acetic acid (IAA) by up to 96%, without affecting the shoot-resident IAA levels. WAT proteins accumulate in cambial vacuoles in an auxin-dependent manner, peaking during night cycles aligned with maximal auxin responses. Depleting active auxin in *wat1 wat2* double mutants triggers broad transcriptomic reprogramming that suppresses cambial proliferation and impairs cell wall remodeling via altered pectin methylesterification. Quantitative data-driven computer model further reveals that WAT proteins function as an intracellular rheostat regulating auxin dynamics across light-dark cycles. Our findings establish that dynamic intracellular compartmentalization fine-tunes local auxin availability in the cambium to ensure robust tree patterning and growth.

INTRODUCTION

Forests cover approximately one-third of the Earth's land surface and play a central role in carbon sequestration, climate regulation, water cycling, and biomass production [1]. Beyond supporting biodiversity, forests and tree crops provide renewable sources of wood and food that underpin the global bioeconomy. Wood accounts for most of the biomass of mature trees and provides the mechanical support and hydraulic transport required for growth. Understanding the mechanisms that regulate wood formation is therefore of major ecological, economic, and biotechnological importance [2].

Wood is produced through secondary growth, a developmental process driven by the vascular cambium, which generates secondary phloem outward and secondary xylem (wood) inward [3]. Following cambial division, xylem cells differentiate through coordinated programs of cell expansion, secondary cell wall deposition, and programmed cell death to produce vessel elements, fibers, and xylem parenchyma. The abundance and organization of these cell types determine wood properties, hydraulic performance, and environmental adaptation [4–5]. Consequently, precise regulation of cambial activity and xylem differentiation determines wood quantity and quality.

Auxin is the principal hormonal regulator of vascular development, secondary growth, and wood formation [6,7]. Polar auxin transport (PAT) of the predominant bioactive auxin, indole-3-acetic acid (IAA), through the vascular cambium establishes the longitudinal and radial auxin gradients that control vascular cambium activity and the differentiation of xylem and phloem cells [8–12]. Although PAT has traditionally been attributed to plasma membrane-localized transporters, growing evidence indicates that intracellular auxin compartmentalization provides an additional layer of regulation of auxin availability [13,14]. However, whether intracellular auxin transport contributes significantly to active auxin availability during secondary growth is an open question. Evidence from poplar (*Populus* spp.) highlights the importance of PAT for wood patterning.

Pharmacological inhibition of PAT in the vascular cambium procude shorter, narrower, and more clustered vessels [15].

One key component of intracellular auxin transport is the tonoplast-localized transporter WALLS ARE THIN1 (WAT1). Initially identified in *Arabidopsis*, WAT1 was first associated with fibers secondary cell wall formation [16] and later shown to export auxin from the vacuole to the cytosol [17]. Despite its role in the intracellaulr auxin transport, *wat1* mutant *in Arabidopsis* displays minor vegetative growth defects and no obvious alterations in vascular organization [16,17]. Similarly, a tomato (*Solanum lycopersicum*) WAT1 homolog regulates secondary xylem formation through a brassinosteroid-BZR1/2-WAT1 regulatory module but has not been implicated in overall plant growth[15].

The hybrid poplar genome (*Populus tremula* × *alba*) contains two WAT1 paralogues, WAT1 and WAT2, whose molecular functions remain unknown. Our single-nucleus transcriptomics identified both genes among the transcripts most strongly associated with drought-induced wood plasticity [5]. Their downregulation under severe drought correlated with the formation of wood with narrower, more numerous vessels, consistent with enhanced hydraulic safety. Likewise, disruption of both paralogues caused severe dwarfism and major defects in xylem patterning, including unusually small vessels, an increased vessel-to-fiber ratio, and disrupted vessel spatial organization, identifying WAT proteins as key regulators of growth and wood formation [5].

Whether WAT regulates tree growth and wood development through intracellular auxin homeostasis remains unknown. Here, we integrated genetics, metabolomics, transcriptomics, cell biology, and quantitative modeling to show that vacuole-localized WAT acts as an intracellular auxin rheostat. By dynamically regulating auxin availability within the poplar vascular cambium, WAT drives vascular cambium activity, primary cell wall formation and robust growth, ultimately ensuring correct wood patterning.

RESULTS

Poplar WAT1 and WAT2 belong to a conserved angiosperm WAT1 paralogous group

Because the molecular function of the two poplar WAT paralogues remains unknown, we first investigated their evolutionary relationships to functionally characterized EamA/WAT1 family members across land plants. The majority of functionally characterized members mediate amino acid transport, whereas auxin transport has only been demonstrated in *Arabidopsis* WAT1 [17,18]. The resulting species tree recovered relationships consistent with established plant evolution (Supplementary Fig. 1). The gene tree resolved multiple EamA/WAT1-related transporter clades, with poplar WAT1 and WAT2 forming a paralogous pair within a conserved angiosperm WAT1 lineage together with *Arabidopsis* WAT1, tomato WAT1, and the *Capsella rubella* ortholog. In contrast, homologs from *Marchantia polymorpha* and *Ceratopteris richardii* fell outside this core lineage, whereas the *Thuja plicata* homolog formed a sister branch. Together, these results place poplar WAT1 and WAT2 within a conserved angiosperm WAT1 lineage containing the functionally characterized *Arabidopsis* WAT1 protein.

WAT1 and WAT2 accumulate in auxin-responsive vascular domains and localize to the tonoplast

Given the previously reported alterations in xylem architecture of *wat1 wat2* mutants [5], we first asked where and when WAT proteins accumulate during stem development and whether their abundance is linked to concentrated auxin responses. To determine the spatial distribution of WAT proteins during stem development, we analyzed two reciprocal complemented lines expressing *pWAT1::WAT1-YFP* together with *pWAT2::WAT2-LUC*, or *pWAT1::WAT1-LUC* together with *pWAT2::WAT2-YFP*, in the *wat1 wat2 #1* double-mutant background. Confocal imaging revealed highly similar accumulation patterns for WAT1-YFP and WAT2-YFP throughout stem

development (Fig. 1A and Supplementary Fig. 2). In young stems (internode 1), fluorescence was predominantly detected in procambial cells and primary xylem. In mature stems (internode 12), both proteins concentrated in the vascular cambium, developing xylem, primary xylem-associated parenchyma, and subsets of xylem ray parenchyma cells (Fig. 1A and Supplementary Fig. 2). These spatial patterns align with our previously reported single-nucleus transcriptomic atlas of poplar stems [5] and closely overlap with the high auxin-response domain in the stem [19].

We next investigated whether WAT protein accumulation is temporally regulated in mature stem tissues (internodes 15-20) using the LUC reporter. Excising stem internodes, thereby interrupting shoot-derived auxin supply through PAT, reduced reporter activity to basal levels: WAT1-LUC showed no rhythmic accumulation, while WAT2-LUC displayed weak, rapidly dampening oscillations (Fig. 1B). Conversely, exogenous application of the synthetic auxin 1-naphthaleneacetic acid (NAA) restored robust, sustained diurnal oscillations, with WAT accumulation peaking near the end of the dark period before rapidly declining after dawn (Fig. 1B). Quantifying endogenous transcript abundance confirmed that *WAT1* and *WAT2* follow night-peaking diurnal expression cycles in wild-type stems, whereas their expression remained low in the *wat1 wat2* double mutant (Fig. 1C). Furthermore, mining single-nucleus RNA-seq atlases of poplar stems[5,20] identified poplar homologs of key auxin-signaling components (*ARF3*, *ARF8*, and *AFB2*). We found that they exhibited diurnal expression patterns co-peaking at night with *WAT1* and *WAT2* (Fig. 1D).

To determine subcellular localization, fluorescently tagged constructs were transiently expressed in *Nicotiana benthamiana* epidermal cells. Expression of *35S::WAT2-linker-eGFP* produced characteristic bulb-like structures in epidermal cells and isolated protoplasts, a well-described artifact of dimerizing GFP targeted to the tonoplast [21] (Supplementary Fig. 3). Replacing eGFP with monomeric GFP (mGFP [21]) largely eliminated bulb formation while preserving membrane-

associated fluorescence (Fig. 1E and Supplementary Fig. 3). The spatial relationship between mGFP signal and chloroplast autofluorescence in intact cells and protoplasts confirmed that WAT1 and WAT2 localize to the tonoplast of the vacuole (Fig. 1E and Supplementary Fig. 3).

Together, these results demonstrate that WAT1 and WAT2 are tonoplast-localized auxin transporters whose expression and protein accumulation are dynamically sustained by shoot-derived auxin across the diurnal cycle. This data supports a model in which vacuolar auxin transport could controls spatiotemporal auxin availability during secondary stem growth.

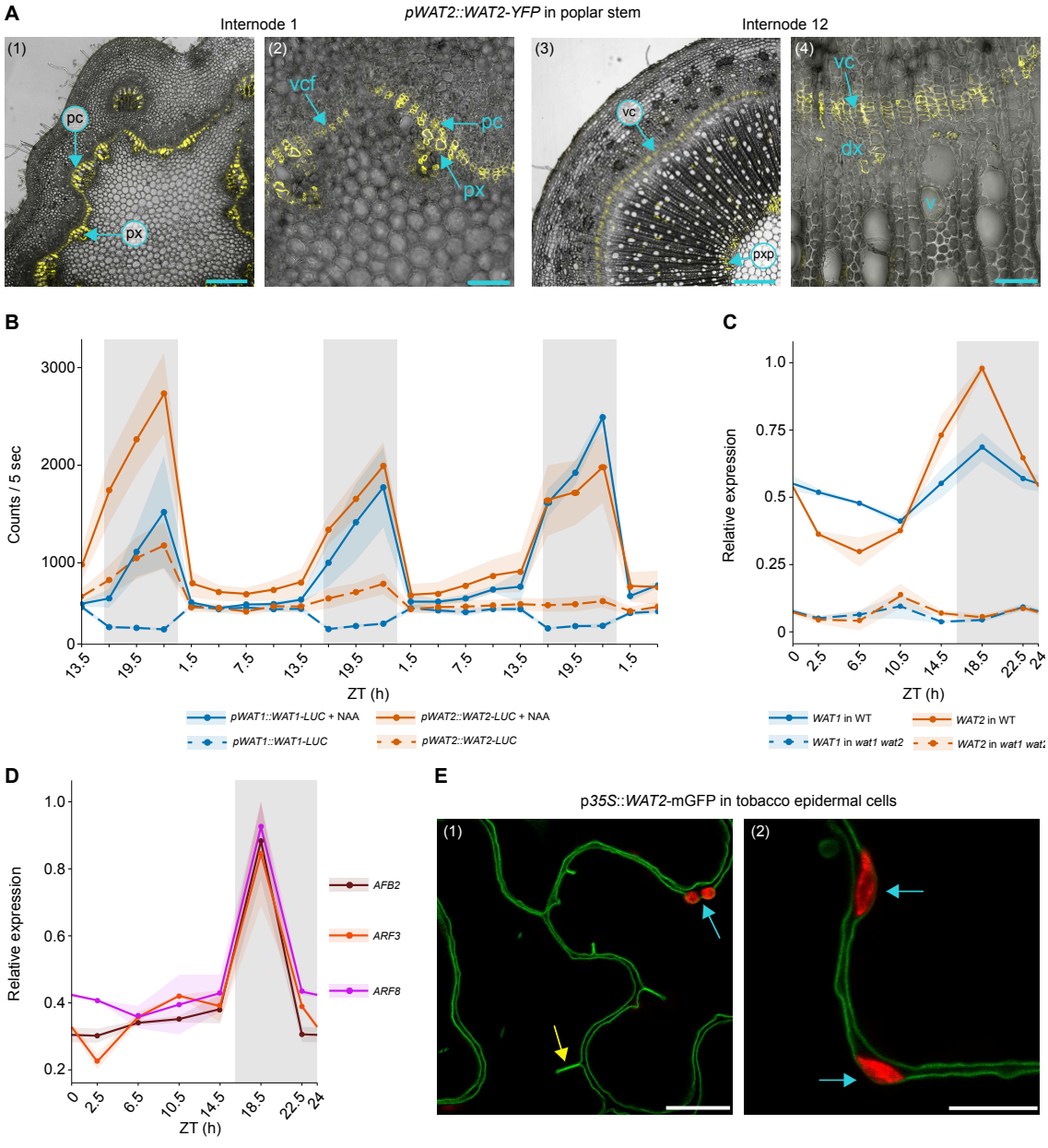


Fig. 1. WAT2 accumulates in vascular tissues, responds to auxin, and localizes to the tonoplast. A Activity of the *pWAT2::WAT2-YFP* in transgenic poplar stems. Representative confocal images of transverse sections from internodes 1 (A1-A2) and 12 (A3-A4). YFP fluorescence was detected in procambial cells, developing xylem, vascular cambial founder cells, vascular cambium, and primary xylem-associated parenchyma. Abbreviations: dx, developing xylem; pc, procambium; px, primary xylem; pxp, primary xylem-associated parenchyma; vcf, vascular cambial founder cells; v, vessel; vc, vascular cambium. Scale bars, 260 μm (A1, A3) and 50 μm (A2, A4). **B** Luminescence of *pWAT1::WAT1-LUC* and *pWAT2::WAT2-LUC* reporters in mature internodes (15-20) over three diurnal cycles under long-day conditions with or without exogenous NAA. Shaded regions indicate the dark period. Data represent mean ± SE from three independent experiments. **C** Diurnal expression of *WAT1* and *WAT2* in WT and *wat1 wat2* stems determined by RT-qPCR. Shaded regions indicate the dark period. WT values represent mean ± SE of two biological replicates; *wat1 wat2* values represent mean ± SE of one biological replicate from each independent mutant line (*wat1 wat2* #1 and #9). **D** Diurnal expression of auxin-response-related genes in WT stems determined by RT-qPCR. Shaded regions indicate the dark period. Data represent mean ± SE of two biological replicates. **E** Subcellular localization of WAT2 in *Nicotiana benthamiana* epidermal cells transiently expressing *35S::WAT2-mGFP*. Chloroplast autofluorescence (cyan arrows) lies outside the GFP signal, indicating tonoplast localization. Yellow arrow in (1) indicates the tonoplast surrounding the transvacuolar strands [16]. Scale bars, 25 μm (E1) and 10 μm (E2).

WAT1 and WAT2 redundantly sustain growth and wood patterning in poplar

The accumulation of both WAT proteins in developing vascular tissues suggested that they may have overlapping functions during secondary growth. To test their contribution to tree growth and wood patterning, we analyzed wild-type (WT), two independent *wat1 wat2* double-mutant lines (*wat1 wat2* #1 and #9), and reciprocal complemented lines (Fig. 2A). The severe dwarf phenotype of *wat1 wat2* mutants, characterized by significantly reduced plant height and stem diameter, was fully rescued in the complemented lines, confirming that these growth defects stem specifically from the combined loss of WAT1 and WAT2 function (Fig. 2A). Anatomical examination revealed stage-dependent developmental defects across stem internodes. Transverse sections of young internodes (internode 1; toluidine blue) preserved overall vascular organization in *wat1 wat2*

stems, despite smaller primary xylem vessels that were restored in the complemented lines (Fig. 2B). In contrast, mature internodes (internode 12; alcian blue/safranin) displayed markedly pronounced defects: as previously reported [5], *wat1 wat2* mutants exhibited disrupted secondary xylem organization and a 110-115% increase in the vessel-to-fiber ratio relative to wild-type (Fig. 2A, B). Both reciprocal complemented lines completely restored xylem organization and the vessel-to-fiber ratio to wild-type levels (Fig. 2A, B).

To evaluate functional redundancy, single complementation lines expressing either *WAT1* or *WAT2* under native promoters were generated in the *wat1 wat2* #1 background. Expression of either gene alone was sufficient to rescue plant height and stem diameter to WT levels (Supplementary Fig. 4). While overall spatial patterning and vessel expansion were markedly improved compared to the double mutant, occasional short radial files of adjacent vessels persisted, resulting in only a partial restoration of the vessel-to-fiber ratio (Supplementary Fig. 4).

Together, these results demonstrate that WAT1 and WAT2 function redundantly to sustain overall tree growth and establish proper wood patterning in hybrid poplar.

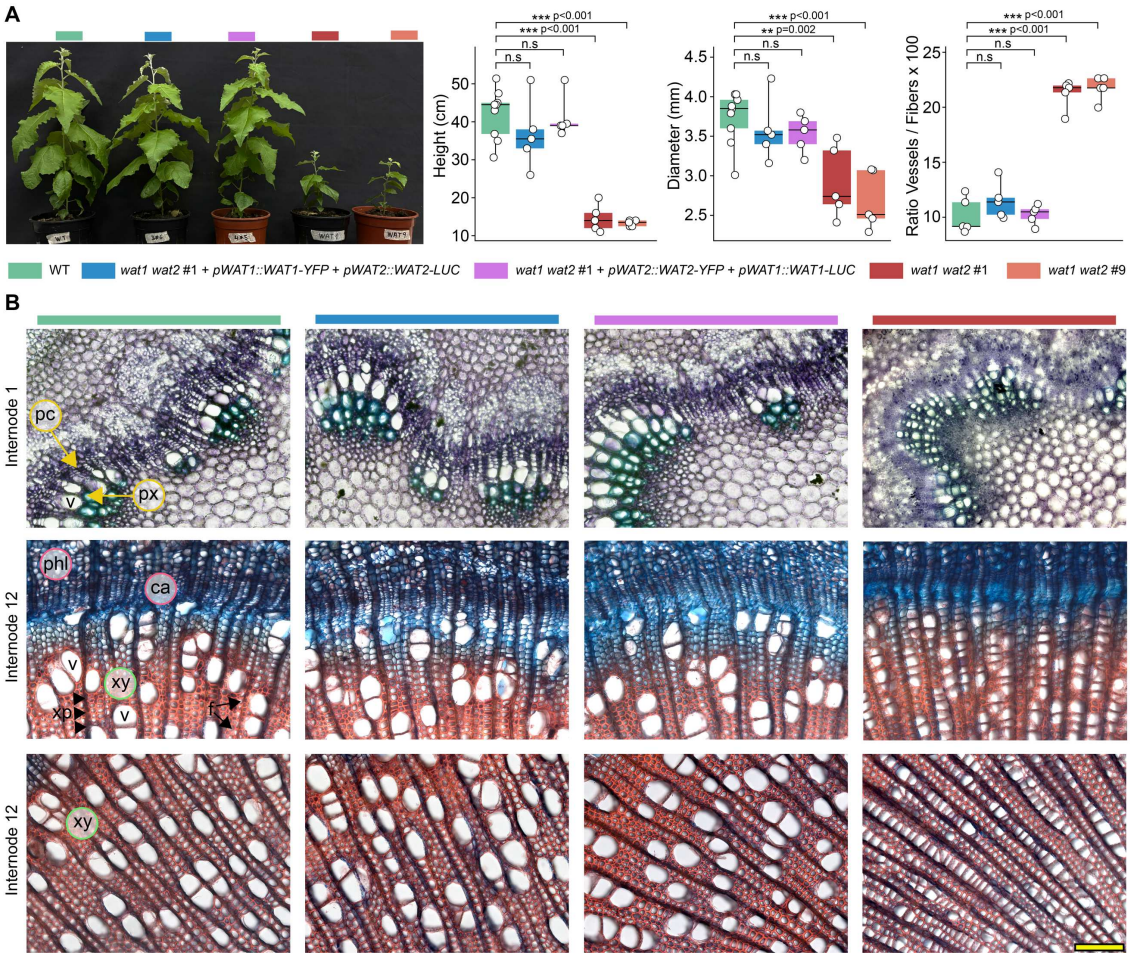


Fig. 2. Reciprocal complementation restores growth and wood development in *wat1 wat2* poplar stems. A Representative phenotype of WT, two independent *wat1 wat2* double-mutant lines (*wat1 wat2* #1 and *wat1 wat2* #9), and two reciprocal complemented lines expressing *pWAT1::WAT1-YFP* + *pWAT2::WAT2-LUC* or *pWAT2::WAT2-YFP* + *pWAT1::WAT1-LUC* in the *wat1 wat2* #1 background. Quantification of plant height, stem diameter, and vessel-to-fiber ratio is shown on the right. Data are presented as the mean ± SE with individual biological replicates shown as dots. Statistical significance was determined by one-way ANOVA followed by Dunnett's post hoc test comparing each genotype with WT (n.s., not significant; **P < 0.01; ***P < 0.001). **B** Representative transverse stem sections from WT, complemented lines, and *wat1 wat2* mutants at internode 1 (top row) and internode 12 (middle and bottom rows). Sections were stained with toluidine blue (internode 1) or alcian blue/safranin (internode 12). WT and complemented plants developed abundant secondary xylem composed predominantly of fibers interspersed with vessels. In contrast, *wat1 wat2* stems exhibited markedly reduced radial growth and a relative increase in vessel abundance, resulting in a substantially higher vessel-to-fiber ratio. The bottom row highlights the altered organization of mature secondary xylem in the mutant stems, showing reduced vessel diameter and altered xylem architecture.

Abbreviations: ca, cambium; f, fiber; phl, phloem; pc, procambium; px, primary xylem; v, vessel; xp, xylem parenchyma; xy, secondary xylem. Scale bars, 100 μm in B.

WAT1 and WAT2 are required to maintain free auxin levels in poplar stems

The tonoplast localization of WAT proteins, together with their auxin-dependent accumulation and strong vascular phenotype, suggested that WAT1 and WAT2 may regulate intracellular auxin homeostasis during secondary growth. To test this hypothesis, we performed targeted metabolite profiling of auxin precursors, biosynthetic intermediates, free IAA, and conjugated derivatives in stem tissues from WT and two independent *wat1 wat2* double-mutant lines (*wat1 wat2* #1 and #9) (Fig. 3A). While levels of early precursors and biosynthetic intermediates showed no consistent differences between WT and mutant stems, free IAA was dramatically reduced in both mutant lines, decreasing by 90% in *wat1 wat2* #1 and 94% in *wat1 wat2* #9 relative to WT (Supplementary Fig. 5). Stem auxin depletion was accompanied by the accumulation of vacuole-associated auxin amino acid conjugates (IAA-AAs) [13]. Specifically, IAA-glutamate levels increased 3.5-fold in *wat1 wat2* #1 and 2.8-fold in *wat1 wat2* #9 relative to WT, While levels of early precursors and biosynthetic intermediates, including tryptophan, indole-3-pyruvic acid (IPyA), and indole-3-acetonitrile (IAN), showed no consistent differences between WT (Supplementary Fig. 5).

To determine how WAT1 and WAT2 contribute to auxin homeostasis along the stem axis, auxin-related metabolites were quantified in the shoot apex, internode 5, and internode 10 of the same genotypes. Free active auxin was unchanged in the shoot apex across all genotypes (Fig. 3B). In contrast, free auxin was nearly abolished throughout the stem axis, dropping by 95% in internode 5 and 95-96% in internode 10 relative to WT (Fig. 3B and Supplementary Fig. 5). Complemented lines substantially restored free IAA accumulation, elevating free auxin 6- to 14-fold over mutant levels (Fig. 3B). IAA-AAs accumulated to higher levels in both mutant lines than in the WT,

reaching statistical significance in internode 10**,** whereas conjugate levels were restored toward WT values in the complemented lines (Fig. 3B). In contrast, early precursors and biosynthetic intermediates, remained largely unchanged, while anthranilic acid showed only minor tissue-specific reductions in the mutants (Supplementary Fig. 6 and 7). Although tryptamine accumulated in developing mutant internodes, free auxin remained severely depleted, indicating that stem auxin loss does not result from impaired biosynthesis (Supplementary Fig. 6 and 7).

We next examined whether loss of WAT function altered the expression of genes involved in polar auxin transport (PAT). RNA-seq analysis of WT stems and *wat1 wat2* stems at ZT8 and ZT23 revealed no widespread transcriptional changes across canonical components of PAT such as PIN, AUX/LAX, and ABCB family members (Supplementary Table 1). Among these transporters, only a *LAX3*-like auxin influx carrier (PtXaAlbH.05G131400) was repressed and a *PIN7*-like transporter (PtXaAlbH.14G119600) was induced in the mutants (Supplementary Table 1).

Together, these findings demonstrate that WAT1- and WAT2-mediated vacuolar auxin transport is required to maintain stem free IAA pools independently of major changes in auxin biosynthesis or the canonical PAT machinery.

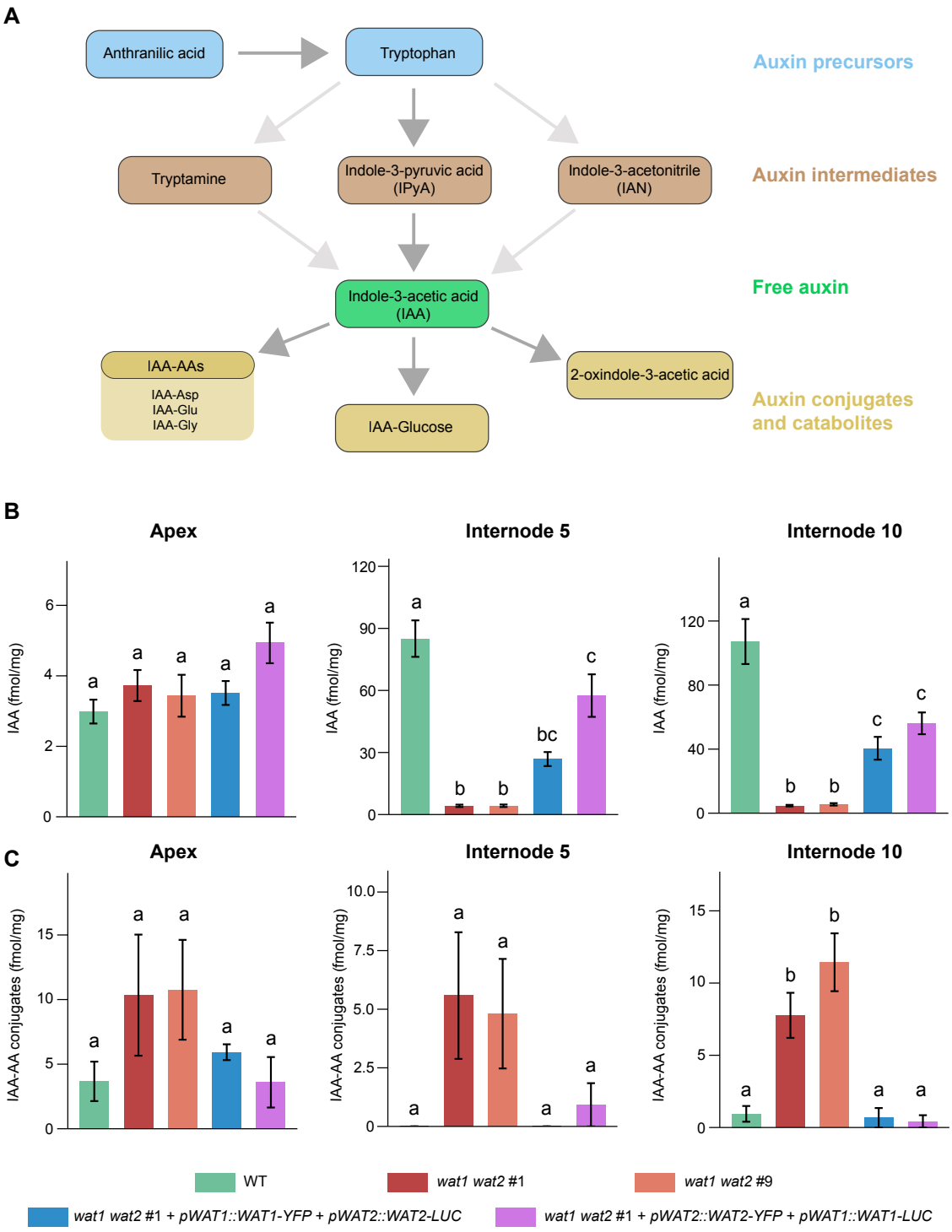


Fig. 3. WAT1 and WAT2 are required to maintain auxin homeostasis in poplar stems. A Schematic representation of the auxin-related metabolites quantified in this study. Metabolites were grouped into biosynthetic precursors, biosynthetic intermediates, free IAA, and IAA conjugates and catabolites. Darker grey arrows indicate the major tryptophan-dependent pathway of IAA biosynthesis via indole-3-pyruvic acid (IPyA). **B** Quantification of free

indole-3-acetic acid (IAA) in the shoot apex, internode 5, and internode 10 of WT, two *wat1 wat2* double-mutant lines (*wat1 wat2* #1 and *wat1 wat2* #9), and two reciprocal complemented lines expressing *pWAT1::WAT1-YFP* + *pWAT2::WAT2-LUC* or *pWAT2::WAT2-YFP* + *pWAT1::WAT1-LUC* in the *wat1 wat2* #1 background. Free IAA levels were strongly reduced in stem tissues of both mutant lines, whereas no significant differences were detected in the shoot apex. Reciprocal complementation partially restored IAA accumulation in internodes 5 and 10. **C** Quantification of IAA-amino acid conjugates (IAA-AAs) in the shoot apex, internode 5, and internode 10 of the indicated genotypes. IAA-AA levels tended to accumulate in *wat1 wat2* stems and reached significantly higher levels in internode 10. Conjugate levels were largely restored toward wild-type values in the complemented lines. Data are presented as the mean ± SE (WT and *wat1 wat2* mutant lines, n = 4 biological replicates; complemented lines, n = 3 biological replicates). Different letters indicate statistically significant differences among genotypes within each tissue as determined by one-way ANOVA followed by Holm-adjusted pairwise comparisons ($P < 0.05$).

Loss of WAT function reprograms cell type-specific transcription across the secondary xylem lineage

Given the dramatic depletion of active auxin in wat1 wat2 stems, we next asked how loss of WAT-dependent auxin homeostasis affects the transcriptional programs underlying wood formation. Because auxin signaling, wood formation, and WAT protein accumulation are temporally regulated [22,23], we performed RNA-seq on stems harvested at ZT8 and ZT23 and analyzed differential expression using a generalized linear model with ZT as a covariate (see Methods). This approach enabled identification of genotype-dependent transcriptional changes while accounting for time-of-day effects, revealing 2,792 downregulated and 3,138 upregulated genes consistently altered in two independent *wat1 wat2* #1 and wat1 wat2 #9 lines relative to wild-type (FDR ≤ 0.05; Supplementary Tables 2 and 3). Gene Ontology (GO) over-representation analysis of downregulated genes revealed broad repression of biological processes associated with growth, hormone signaling, and cell wall formation (Fig. 4A and Supplementary Tables 4 and 5). Consistently, Gene Set Enrichment Analysis (GSEA) confirmed significant repression of

pathways related to cell division and protein translation in the mutant lines (Supplementary Fig. 8 and Supplementary Tables 6 and 7).

To resolve these transcriptional responses at cellular resolution, we deconvoluted the bulk RNA-seq dataset using BayesPrism [24], using our previously published poplar stem single-nucleus RNA-seq atlas [20] as a reference. This approach estimated cell type-specific transcriptional changes in the mutants relative to WT from the bulk RNA-seq data across the major wood-forming cell populations, spanning the cambium-to-xylem developmental continuum: cambial zone (CZ), proliferative/cells undergoing replication (CR), xylem mother cells and juvenile xylem (XMC/JX), mature xylem (MX), and xylem parenchyma (XP) (Fig. 4B, C and Supplementary Tables 8 and 9). The strongest WAT-dependent transcriptional changes occurred in CZ and CR, where genes involved in cell-cycle progression, ribosome biogenesis, and translation were repressed in the mutants (Fig. 4C and Supplementary Tables 10 and 11).

In juvenile xylem (XMC/JX), mutants exhibited marked repression of genes involved in pectin biosynthesis and remodeling (Fig. 4C and Supplementary Tables 8 and 9), including genes associated with homogalacturonan methylesterification, such as *CGR2* (PtXaAlbH.01G239600) [25], *QUASIMODO2/TSD2* (*QUA2*) (PtXaAlbH.05G124100) [26], and a *PMEI* family member (PtXaAlbH.14G101100) [27], as well as genes involved in pectin biosynthesis and assembly, including *ATKDSA2* (PtXaAlbH.05G152500) [28], *ARAD1* (PtXaAlbH.15G098600) [29], and TMN1/EMP12 (PtXaAlbH.04G169500) [30].

Mature xylem (MX) displayed a transcriptional signature consistent with attenuated xylem maturation, with repression of genes involved in secondary cell wall formation and the shikimate/chorismate pathway in the mutants (Fig. 4C and Supplementary Tables 8 and 9), which supplies precursors for lignin biosynthesis [31]. In contrast, xylem parenchyma (XP) showed the

strongest induction of genes associated with water transport, hormone signaling, and stress adaptation in the mutant stem (Fig. 4C and Supplementary Tables 8 and 9).

Together, these analyses reveal that WAT loss reprograms the secondary xylem lineage in a highly cell type-specific manner: suppressing proliferative programs in the cambium, pectin biosynthesis and remodeling in developing xylem, and maturation programs in mature xylem, while activating adaptive stress responses in xylem parenchyma.

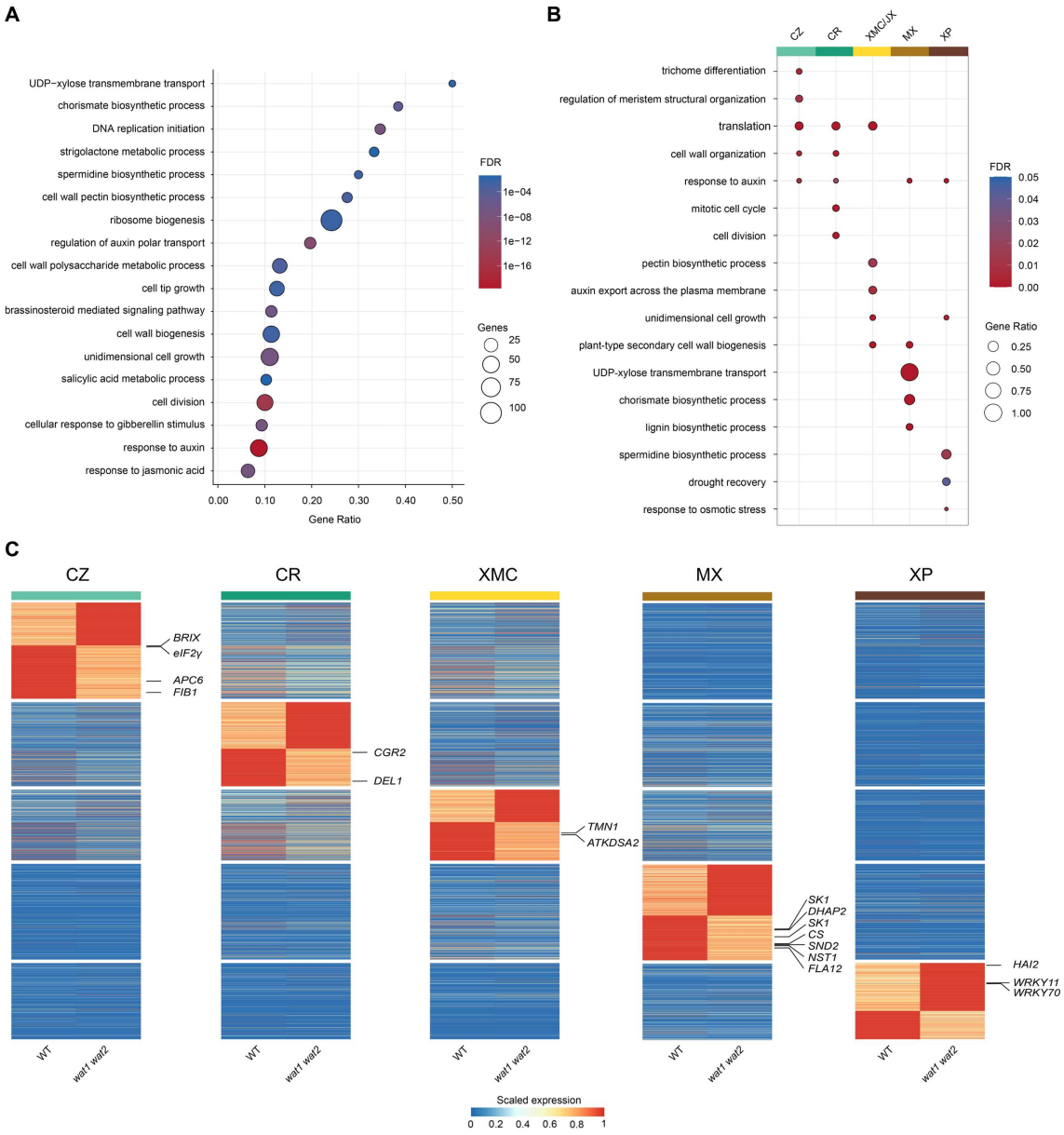


Fig. 4. WATs-dependent auxin homeostasis sustains proliferative, translational and cell-wall associated programs across the wood-forming lineage. A Gene Ontology (GO) over-representation analysis of genes consistently downregulated in both *wat1 wat2* mutants relative to WT. Enriched biological processes included auxin responses, cell division, ribosome biogenesis, cell wall polysaccharide metabolism, pectin biosynthesis, and chorismate biosynthesis. Dot size indicates the number of genes associated with each term, and color represents the false discovery rate (FDR). **B** Cell type-specific GO enrichment analysis of downregulated genes obtained by deconvolution of bulk RNA-seq data using BayesPrism and a previously published poplar stem single-nucleus RNA-seq atlas. Five populations spanning the cambium-to-xylem developmental continuum were analyzed: cambial zone (CZ), proliferative/cell replication cells (CR), xylem mother cells and juvenile xylem (XMC/JX), mature xylem (MX), and xylem parenchyma (XP). Dot size represents the gene ratio and color indicates the FDR. **C** Heatmaps showing representative cell type-specific genes differentially expressed between WT and *wat1 wat2* stems within each population. Heatmap colors represent scaled expression values independently for each gene.

Altered wood formation is associated with reduced pectin methylesterification but unchanged secondary wall composition

The repression of pectin biosynthesis and remodeling programs in developing xylem suggested that altered primary cell wall properties may contribute to the wood patterning defects of *wat1 wat2* mutants. We therefore monitored the expression of representative genes involved in pectin modification and chorismate biosynthesis throughout the daily cycle. In WT stems, the poplar homolog of the pectin methyltransferase *QUA2* and the chorismate pathway genes *DAHPS2* and *SHIKIMATE KINASE1* exhibited diurnal expression patterns, whereas transcript levels were consistently reduced and temporal regulation was attenuated in *wat1 wat2* stems (Fig. 5A).

To validate the alterations in pectin metabolism identified in both bulk and deconvoluted transcriptomes, we examined homogalacturonan methylesterification in mature stem cross-sections using the JIM7 monoclonal antibody. Consistent with the repression of genes involved in homogalacturonan biosynthesis and methylesterification, JIM7 immunofluorescence was

significantly reduced in the cambial zone and developing xylem of *wat1 wat2* stems compared with WT (Fig. 5B, C). Finally, we compared secondary wall properties independently of developmental stage, by growing WT and *wat1 wat2* plants until they reached a comparable height (1 m), and collected the basal 20 cm of the stem for secondary cell wall analysis. Whereas WT plants reached this height after approximately two months, *wat1 wat2* mutants required more than nine months. Despite this marked developmental delay and pronounced defects in radial growth, cambial activity, and pectin methylesterification, no significant differences were detected in lignin, cellulose, or hemicellulose content between WT and mutant stems (Fig. 5D, E). Likewise, fiber and vessel wall thickness as well as fiber area were unaffected, whereas vessel area was strongly reduced and vessel distribution markedly altered in the mutants (Fig. 5D-F).

Together, these results validate WAT-dependent regulation of pectin methylesterification and demonstrate that WAT-mediated auxin homeostasis preferentially controls early events such as cambial activity and vessel patterning, likely by regulating pectin-dependent primary cell wall remodeling during cell expansion, and unlike *Arabidopsis* and tomato, without altering fiber differentiation or secondary cell wall formation. Our findings reveal a distinct role for WAT proteins during tree secondary growth, highlighting species-specific and cell-type-specific auxin requirements among the developmental programs that shape growth and wood formation.

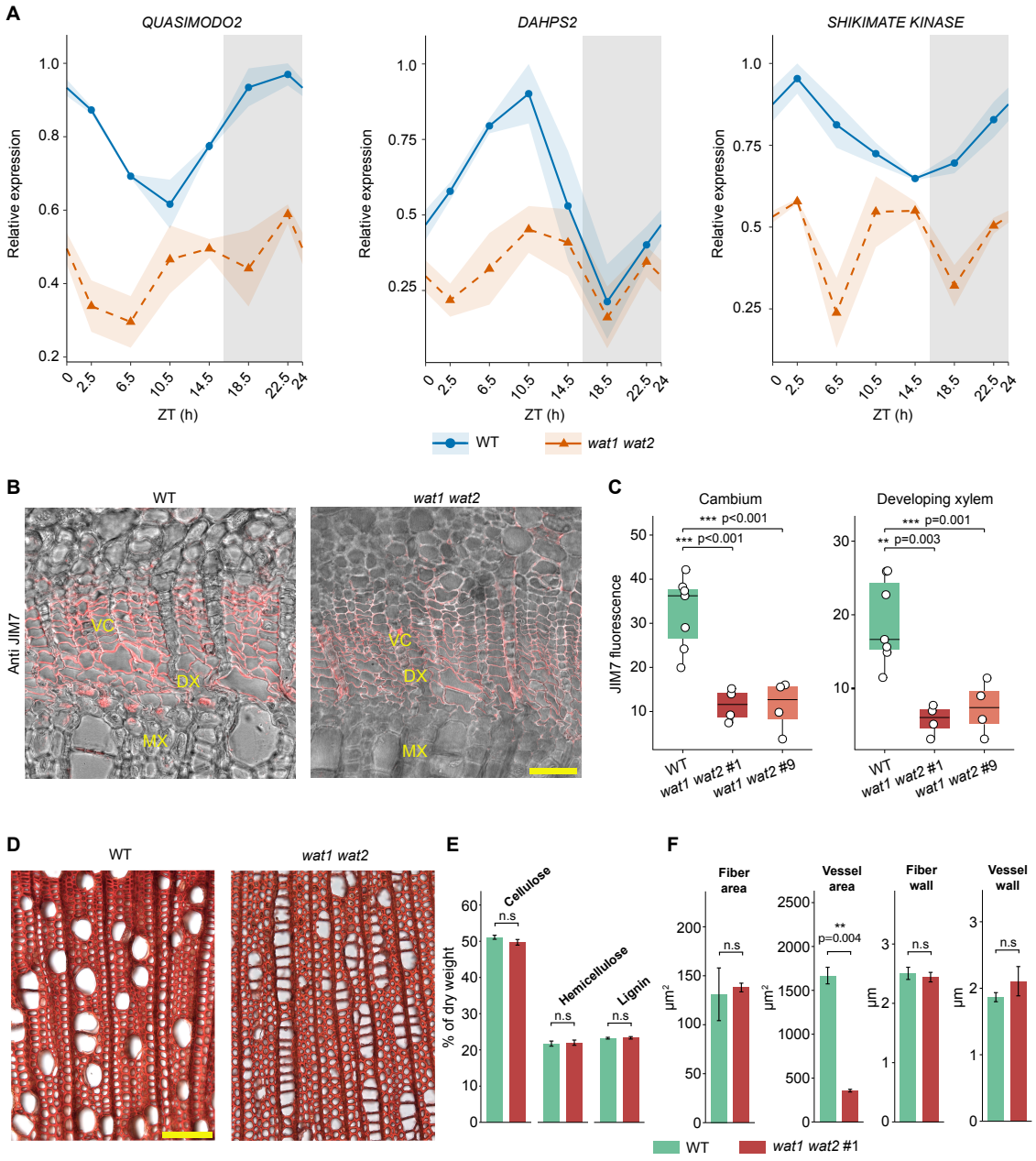


Fig. 5. WAT-mediated auxin homeostasis is required for pectin methylesterification and vascular patterning. **A** Diurnal expression of representative genes involved in pectin methylation and chorismate biosynthesis in mature stems. *QUASIMODO2*, *DAHPS2*, and *SHIKIMATE KINASE1* exhibited diurnal oscillations in WT, whereas expression was reduced in *wat1 wat2*. Shaded areas indicate the dark period. WT values represent mean ± SE of two biological replicates; *wat1 wat2* values represent mean ± SE of one biological replicate from each independent mutant line (*wat1 wat2* #1 and #9). **B** Representative confocal images of JIM7 immunolabeling in mature stem cross-sections. JIM7 fluorescence (red), marking highly methylesterified homogalacturonan, is reduced in the vascular cambium

(VC) and developing xylem (DX) of wat1 wat2 stems. MX, mature xylem. Scale bar, 50 µm. **C** Quantification of JIM7 fluorescence intensity in VC and DX. Boxplots show individual replicates. One-way ANOVA with Dunnett's post hoc test. ***P < 0.001. **D** Representative stem cross-sections from WT and wat1 wat2 plants harvested at comparable height (~1 m). Despite the prolonged growth period of mutants, secondary wall organization appeared preserved. Scale bar, 100 µm. **E** Lignin, cellulose, and hemicellulose contents in the basal 20 cm (mean ± SD; n = 5 WT, n = 10 wat1 wat2 #1). Welch's t-test. **F** Quantification of fiber area, vessel area, fiber wall thickness, and vessel wall thickness (mean ± SD; n = 3). Vessel area was reduced in wat1 wat2 stems, whereas fiber area and wall thickness were unchanged. Welch's t-test. **P < 0.01; ***P < 0.001.

Quantitative modeling reveals how WAT gene dosage regulates intracellular auxin compartmentalization

Our experimental data revealed several key insights into WAT function during wood development in poplar. WAT proteins localize to the vacuolar membrane (tonoplast), and *wat1 wat2* mutants exhibit elevated levels of vacuole-associated auxin conjugates accompanied by up to a 96% reduction in free active auxin. This data indicates that WAT transporters export auxin from the vacuole to strictly regulate the active cytosol pool, a mechanism further supported by our metabolomics dataset. However, the mechanistic core of how WAT controls the intracellular auxin reservoir in cambial cells is unclear.

To understand better this mechanism, we constructed a quantitative computational model of intracellalar auxin distribution in a cambial cell (Fig. 6A). Our model incorporates subcellular compartments (extracellular space, cytosol, and vacuole) defined by distinct pH states, alongside active (free IAA) and inactive (IAA-conjugated) auxin pools (see Methods). Polar auxin transport (PAT) across the plasma membrane is mediated by PAT components that include both efflux and influx auxin carriers. Intracellular exchange across the tonoplast interface is driven by WAT-mediated efflux and a hypothetical influx carrier required for active transport against the

383 electrochemical gradient. Expression levels of all transporters at the vascular cambium were
384 inferred from snRNA-seq transcriptomic data [20], while known parameters such as transport rates
385 and dissociation constants were taken from literature reports (see Methods). Missing parameters
386 were identified by fitting the model against our metabolomics data on free active and conjugated
387 auxin levels in wild-type and *wat1 wat2* mutants (Supplementary Fig. 5).
388 Calibrated model simulations revealed that WAT gene dosage controls the gradual transition from
389 a high active auxin pool in WT (Fig. 6B; Supplementary Fig. 9A-D, Supplementary Movie 1) to a
390 low active auxin pool in the mutant (Fig. 6C, Supplementary Movie 2), centered around a crossover
391 point corresponding to half of the WT active auxin concentration (Fig. 6C). This phenomenon is
392 driven by a balance between vacuolar auxin influx and efflux (Supplementary Fig. 10A, B).
393 Notably, the model predicted that the active auxin pool drops linearly with decreasing WAT gene
394 expression, followed by a non-linear increase in the inactive pool above the crossover threshold at
395 approximately 5% of active WAT (Fig. 6D). Plotting active versus inactive auxin pools across
396 varying WAT gene dosages and overlaying experimental observations illustrated the inner
397 workings of this mechanism (Fig. 6E). Specifically, WAT precisely tunes how much auxin remains
398 in the active pool available for signaling versus how much is sequestered inside the vacuole in an
399 inactive conjugated state (Fig. 6E). This mechanism resembles a molecular rheostat or
400 potentiometer that finely controls active auxin dosage (Fig. 6E). The global sensitivity analysis
401 revealed that key parameters influencing active vs inactive auxin pool distribution primarly relate
402 to WAT transport and auxin degradation kinetics (Supplementary Fig. 11A, B).
403 These findings complement our experimental observations by establishing an intuitive regulatory
404 mechanism through which WAT tunes intracellular auxin availability in the cambium as WAT
405 expression levels fluctuate across diurnal cycles. The model also explains how reduced WAT
406 dosage drives a dramatic depletion of active auxin, underscoring its pivotal role in directing

vacuolar auxin flux into the cytosol, but also consequences for PAT-driven long distance transport across adjacent cells. Together, these results highlight the necessity of tight cell-autonomous control of auxin homeostasis for proper vascular cambium function.

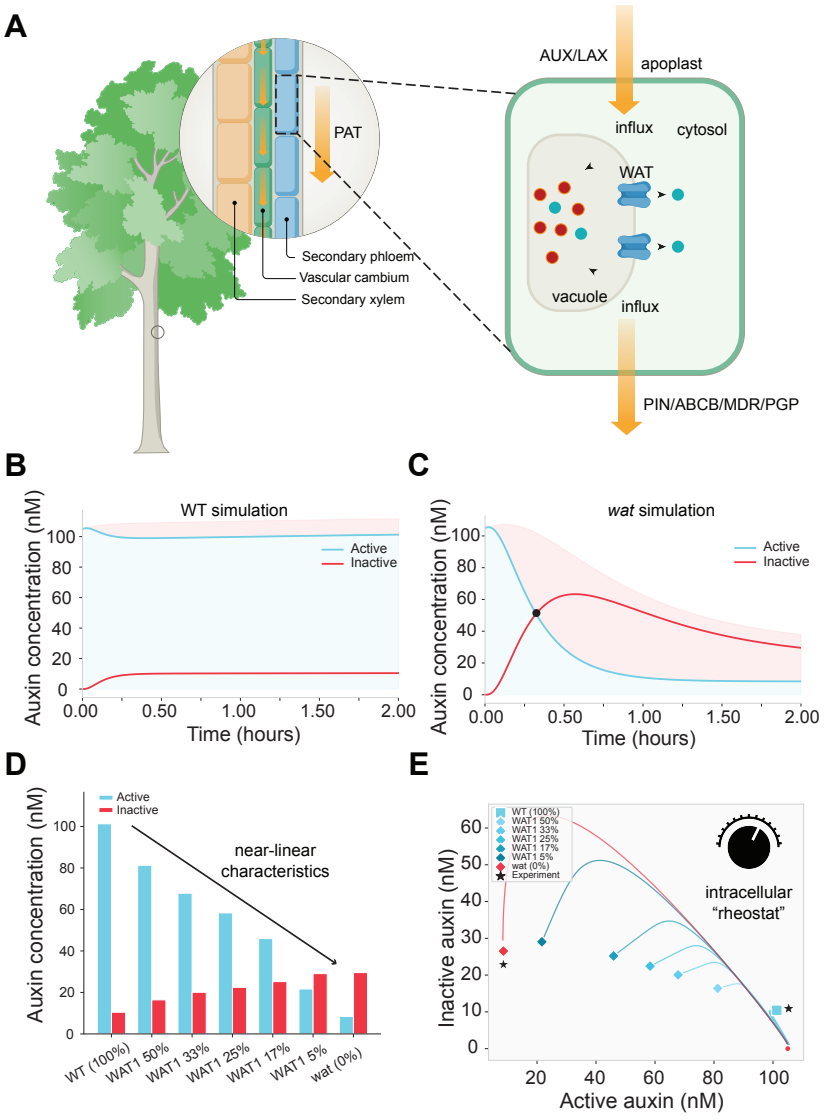


Fig. 6. Model of intracellular rheostat controlling cambium auxin levels. A Schematic of the intracellular auxin transport model in the poplar cambium cell. WAT transporters control the tonoplast border by alternating both active (cyan circles) and inactive auxin pools (red circles). **B** Simulation of wild-type scenario shows that active auxin dominates over inactive auxin storage in the presence of intact WAT transporters. **C** Predicted auxin concentrations in simulated *wat* mutant. Note a switch toward inactive auxin dominance at the cross point (black circle). **D**

Relationship between WAT gene dosage and auxin concentrations. **E** Mechanism of intracellular rheostat fine-tunes active auxin availability in the cambium cell.

DISCUSSION

While polar auxin transport (PAT) through the vascular cambium is known to drive cambial activity and patterning, how intracellular auxin distribution contributes to these processes remains poorly understood. Here, we show that poplar WAT proteins, expressed in the vascular cambium, maintain nearly 95% of active cambial auxin without altering shoot apex biosynthesis. Despite this severe free IAA depletion in *wat1 wat2* stems, inactive amino acid conjugates [32] were elevated relative to WT plants, signaling a shift toward an inactive storage state. Experimental and computational modeling data support a mechanism in which auxin continuously cycles between the cytosol and the vacuole within cambial cells. We propose that WAT transporters recycle vacuolar auxin back to the cytosol, thereby maintaining the signaling-competent auxin pool required for both intracellular signaling and PAT. In the absence of WAT activity, auxin entering the vacuolar pathway is no longer efficiently recycled and progressively exits the active pool, becoming progressively enriched as inactive conjugates before ultimately being degraded. Although the molecular mechanisms governing these metabolic conversions remain to be elucidated, this intracellular rheostat provides a quantitative framework explaining how loss of WAT activity causes the dramatic depletion of free auxin observed in *wat1 wat2* stems, ultimately impairing the active auxin pool required to maintain the steep auxin gradients that govern vessel size and patterning in the cambial zone [15]. Importantly, the model predicts that loss of WAT activity alone suffices to reproduce the dramatic depletion of active auxin within a single cambial cell, without requiring progressive auxin loss across successive cells along the PAT route. This suggests that cell-autonomous WAT activity locally determines how much auxin remains available

for signaling whereas cell-to-cell transport ensures that excess auxin is evenly distributed down the stem.

This depletion suppressed cambial division, cell cycle progression, ribosome biogenesis, and translation-associated genes, echoing known effects of reduced auxin signaling in hybrid aspen [6]. This translational suppression likely reflects impaired auxin-TOR signaling[33–35] and highlights translational regulation as an integral component of xylem cell fate and vascular development [36]. Furthermore, *wat1 wat2* mutants exhibited reduced homogalacturonan methylesterification, a key driver of primary cell wall mechanics and active cambial growth [25,37,38], while secondary wall thickness and composition (lignin, cellulose, hemicellulose) remained unaffected. Thus, unlike in *Arabidopsis*, tomato, and cotton, where WAT1 drives secondary cell wall deposition [17,39,40], poplar WAT proteins regulate early developmental events determining wood architecture.

Remarkably, a 90-96% reduction in free stem IAA selectively disrupted vessel size and patterning while preserving fiber differentiation and secondary wall deposition, pointing to distinct auxin sensitivities among secondary xylem cell types. This patterning mechanism is linked to nocturnal accumulation of WAT proteins that buffers daily fluctuations in auxin availability during secondary xylem development [22,23].

Given the rising threat of drought under climate change and the importance of vascular plasticity for stress adaptation, uncovering how the intracellular auxin rheostat tunes vascular architecture provides both a mechanistic framework for bioengineering climate-resilient trees with minimal growth penalties.

METHODS

Plant material and growth conditions

Hybrid poplar (*Populus tremula* × *alba* INRA clone 717-1B4) was propagated in vitro from shoot tips and stem cuttings on Murashige and Skoog (MS) medium supplemented with 2% sucrose, 0.5 mg L^{-1} indole-3-acetic acid, 0.5 mg L^{-1} indole-3-butyric acid, and 0.7% (w/v) agar (pH 5.7). Plants were maintained under long-day conditions (16 h light/8 h dark) at 22°C, 65% relative humidity, and 100 µmol m^{-2} s^{-1} photosynthetic photon flux density. For anatomical analyses, auxin metabolite profiling, RNA-seq, and cell wall analyses, plants were transferred to soil and grown under the same conditions.

Anatomical analysis

For the anatomical analysis shown in Fig. 1, stem internodes 1 and 12 were collected from six-week-old WT, *wat1 wat2* double mutants, and complemented lines. Internode 1 was defined as the stem segment between the first and second fully expanded leaves below the apex. Samples were fixed as previously described [38], sectioned (40-60 µm) with a Leica VT1200S vibratome, and stained with Toluidine Blue O (internode 1) or Safranin/Alcian Blue (internode 12). Images were acquired using a Zeiss LSM 880 microscope. Vessel and fiber numbers were quantified from at least two cross-sections per plant (n = 5) using the Analyze Particles function in ImageJ. For the anatomical analysis shown in Fig. 5, the internode immediately above the 20 cm basal portion, which was collected for cell wall composition, was used. For the analysis shown in Supplementary Fig. 1, internode 16 was cut. These portions were fixed, sectioned, stained with Safranin/Alcian Blue, and analyzed in the same way.

Auxin metabolism analyses

Auxin metabolites were quantified by UHPLC-ESI-QqQ-MS/MS at the Swedish Metabolomics Centre (Umeå, Sweden). Two independent analyses were performed. The first included mature stems (internodes 5-15) from WT, *wat1 wat2* #1, and *wat1 wat2* #9 (n = 8 biological replicates per genotype). The second included shoot apices and internodes 5 and 10 from WT, *wat1 wat2* #1, *wat1 wat2* #9, and the two reciprocal complemented lines (Fig. 2), using four biological replicates for WT and mutant lines and three for each complemented line. Samples were extracted, purified, and analyzed as described previously , with minor modifications. Briefly, frozen tissue (20 mg) was extracted in phosphate buffer containing isotopically labeled internal standards, derivatized to stabilize indole-3-pyruvic acid (IPyA), purified by solid-phase extraction, and analyzed using an Agilent 1290 Infinity UHPLC coupled to an Agilent 6495D Triple Quadrupole mass spectrometer. Metabolites were quantified by multiple reaction monitoring (MRM) using isotope dilution and calibration curves generated from authentic standards, and concentrations were expressed as fmol mg^{-1} fresh weight.

RNA sequencing

Total RNA was extracted from mature stems (internodes 10-15) of six-week-old WT, *wat1 wat2* #1, and *wat1 wat2* #9 plants collected at ZT8 and ZT23 (n = 5 biological replicates per genotype and time point) as previously described [42]. Libraries were prepared using the TruSeq Stranded mRNA Library Prep Kit and sequenced on an Illumina NovaSeq X platform by Macrogen (South Korea). Reads were mapped to the *Populus tremula* × *alba* INRA clone 717-1B4 HAP2 v5.1 reference genome using HISAT2.

Differential expression analysis of bulk

Differential expression analysis was performed using edgeR [43]. After filtering lowly expressed genes and performing TMM normalization, a generalized linear model with genotype and sampling time (ZT) as additive factors was fitted. Differential expression was assessed using quasi-likelihood F-tests, and P-values were adjusted using the Benjamini-Hochberg method [44]. Genes with False Discovery Rate (FDR) ≤ 0.05 that were differentially expressed in both *wat1 wat2* mutant lines with the same direction of change were considered differentialy expressed genes (DEGs) and retained for downstream analyses (Supplementary Tables 2 and 3).

Gene Ontology over-representation analysis of DEGs from bulk

Gene Ontology (GO) over-representation analysis was performed separately for the up- and downregulated DEGs using topGO [45]. *Populus tremula* × *alba* HAP2 genes were mapped to *Arabidopsis thaliana* orthologs using the annotation file available at Phytozome for *Populus tremula* × *alba* HAP2, and GO Biological Process annotations were retrieved from TAIR [46]. Enrichment was assessed using the weight01 algorithm with Fisher's exact test, and P-values were adjusted using the Benjamini-Hochberg method [44]. GO terms with FDR ≤ 0.05 were considered significantly enriched (Supplementary Tables 4 and 5).

Construction of the ortholog dictionary *Populus tremula* × *alba HAP2 - Populus trichocarpa*

An ortholog dictionary between *Populus tremula* × *alba* HAP2 [47] and *Populus trichocarpa* [48] was generated from BioMart annotations available in Phytozome [49]. One-to-one and one-to-many orthologs were retained. For many-to-many relationships, the first pair after alphabetical sorting was selected, whereas for many-to-one relationships, only bulk RNA-seq DEGs located on corresponding chromosomes in both species and with the highest WT expression were retained.

Kyoto Encyclopedia of Genes and Genomes Gene Set Enrichment Analysis of bulk differential expression results

Kyoto Encyclopedia of Genes and Genomes (KEGG) [50] pathway enrichment analysis was performed using Gene Set Enrichment Analysis (GSEA) [51]. Differential expression results from the two *wat1 wat2* mutant lines obtained with edgeR [43] were combined by averaging logFC values, and combining P-values using Fisher's method followed by Benjamini-Hochberg correction [44]. Genes were ranked by the signed -log10 of the adjusted P-value. *Populus tremula* × *alba* HAP2 genes were mapped to *Populus alba* (NCBI RefSeq assembly GCF_005239225.2) using reciprocal best hits implemented in DIAMOND [52]. KEGG pathway annotations for *Populus alba* were retrieved using KEGGREST, and GSEA was performed with clusterProfiler [53] using gene sets of 10-500 genes. Pathways with FDR ≤ 0.05 were considered significantly enriched (Supplementary Tables 6 and 7).

Phylogenetic analysis of WAT-related genes

Orthologous proteins of *Populus tremula* × *alba* HAP2 WAT1 (PtXaAlbH.02G025500) and WAT2 (PtXaAlbH.05G183400) were identified from the proteomes of *Marchantia polymorpha*, *Ceratopteris richardii*, *Thuja plicata*, *Solanum lycopersicum*, *Arabidopsis thaliana*, and *Capsella rubella* obtained from Phytozome [49] with OrthoFinder [54]. OrthoFinder performed protein homology searches, multiple sequence alignment, and phylogenetic inference with DIAMOND [52], FAMSA [55], and IQ-TREE, respectively [56]. Evolutionary models were selected using ModelFinder [57], and branch support was assessed with 1,000 ultrafast bootstrap replicates [58]. The species tree and the gene tree containing *Arabidopsis* WAT1 were visualized using iTOL [59].

Validation of hybrid poplar WAT1 and WAT2 localization in poplar stem

DNA constructs were generated using the Golden Gate cloning system [60]. Promoter sequences of 2,021 bp for *WAT1* (PtXaAlbH.02G025500) and 2,023 bp for *WAT2* (PtXaAlbH.05G183400), together with their coding sequences, were synthesized (Integrated DNA Technologies) and fused in-frame to YFP or luciferase (LUC) through a flexible GGGGS linker. The resulting transcriptional units were assembled into the binary vector pAGM4673 (MoClo Toolkit) to generate the constructs p*WAT1*::*WAT1*-linker-YFP + p*WAT2*::*WAT2*-linker-LUC, p*WAT2*::*WAT2*-linker-YFP + p*WAT1*::*WAT1*-linker-LUC, p*WAT1*::*WAT1*-linker-YFP, and p*WAT2*::*WAT2*-linker-YFP. Constructs were introduced into the *Populus tremula* × *alba* 717-1B4 *wat1 wat2* #1 background by *Agrobacterium tumefaciens* (GV3101)-mediated transformation as previously described [61].

Stem internodes 1 and 12 from four-week-old reciprocal complemented lines were fixed, sectioned, and mounted as described above. YFP fluorescence was imaged using a Leica TCS SP8 confocal microscope with 514 nm excitation.

Characterization of the poplar WAT1 and WAT2 daily patterns in the stem

Luciferase activity in mature stems was monitored as previously described for poplar leaves [62]. Stem segments (0.5 cm) from internodes 15-20 of six-week-old *wat1 wat2* #1 + p*WAT1*::*WAT1*-linker-YFP + p*WAT2*::*WAT2*-linker-LUC and *wat1 wat2* #1 + p*WAT2*::*WAT2*-linker-YFP + p*WAT1*::*WAT1*-linker-LUC plants were placed individually in white 96-well plates containing MS 1B medium mented with D-luciferin. Luciferase activity was measured every 3 h (5 s integration time) using a TriStar2 LB 942 luminometer (Berthold Technologies). Three independent experiments were performed.

Subcellular localization of WAT1 and WAT2 in tobacco epidermal cells

Level 2 Golden Gate constructs expressing p35S::*WAT1*-linker-eGFP, p35S::*WAT2*-linker-eGFP, p35S::*WAT1*-linker-mGFP, and p35S::*WAT2*-linker-mGFP were generated as described above. Transient expression in *Nicotiana benthamiana* leaves was performed by *Agrobacterium*-mediated infiltration as previously described [63]. Leaves were collected 3 days after infiltration and imaged directly or following a protoplast isolation protocol [64] with minor modifications. Leaf sections and isolated protoplasts were imaged using a Leica TCS SP8 confocal microscope with 488 nm excitation.

Deconvolution of vascular cell types in bulk

Bulk RNA-seq deconvolution was performed using BayesPrism [24], with *Populus trichocarpa* scRNA-seq data as reference [20].

Populus tremula × *alba* HAP2 genes were converted to their *Populus trichocarpa* orthologs using the ortholog dictionary described above. Cell type-specific marker genes were identified using Seurat FindAllMarkers [65] with a Wilcoxon rank-sum test, retaining only significantly positive markers (adjusted P-value ≤ 0.05). Sieve elements were excluded from the reference due to deconvolution artifacts. BayesPrism was run with default parameters to infer cell type-specific expression profiles.

Differential expression analysis on deconvolved cell type expression

Differential expression analysis of deconvolved cell type-specific expression profiles was performed using the same edgeR pipeline described for the bulk RNA-seq analysis. Analyses were conducted independently for each cell type, comparing WT with *wat1 wat2* #1 and *wat1 wat2* #9.

607 Genes with FDR ≤ 0.05 in both mutant lines were retained and gene identifiers were converted
608 from *Populus trichocarpa* to *Populus tremula* × *alba* using the dictionary described above.
609 To identify cell type-specific marker genes, a one-versus-rest differential expression analysis was
610 performed on WT deconvolved expression profiles. Genes with positive logFC and FDR ≤ 0.05
611 were retained as cell type markers and intersected with the differential expression results from the
612 corresponding cell type to identify genes consistently up- or downregulated DEGs in both *wat1*
613 *wat2* mutant lines in each cell type (Supplementary Tables 8 and 9).
614
615 **Gene ontology over representation analysis of DEGs from deconvolution for each cell type**
616 GO over-representation analysis was performed separately for the up- and downregulated DEGs
617 of each cell type after intersection with their respective cell type-specific markers using the same
618 pipeline described for the bulk RNA-seq analysis except that *Arabidopsis thaliana* orthologs of
619 *Populus trichocarpa* [48] were used instead. GO terms with FDR ≤ 0.05 were considered
620 significantly enriched (Supplementary Tables 10 and 11).
621
622 **qRT-PCR expression analysis**
623 Total RNA was extracted from mature stems of six-week-old WT, wat1 wat2 #1, and wat1 wat2
624 #9 plants as described above. cDNA synthesis, primer design, quantitative RT-PCR, and data
625 analysis were performed as previously described [42]. Primer sequences are listed in Supplementary
626 Table 12.
627
628 **Immunolocalization of methyl-esterified pectins**
629 Immunolocalization of highly methyl-esterified homogalacturonan was performed as previously
630 described [38]. Internode 12 stem sections from six-week-old WT and wat1 wat2 plants were fixed,

sectioned, and stored at -20°C until use. Sections were permeabilized with 0.1% Tween-20 in PBS instead of cellulase digestion, blocked with 5% BSA, and incubated with the JIM7 rat monoclonal antibody (Agrisera), followed by an Alexa Fluor 546-conjugated goat anti-rat IgG secondary antibody. Fluorescence was imaged using a Leica TCS SP8 confocal microscope (561 nm excitation), and mean fluorescence intensity in the vascular cambium and developing xylem was quantified in ImageJ using identical analysis parameters for all samples.

Secondary cell wall composition analysis

Secondary cell wall composition was determined in WT (n = 5) and *wat1 wat2* #1 (n = 10) plants. Secondary xylem was collected from the basal 20 cm of stems once plants reached the same height (1 m). Because of the severe growth defect of *wat1 wat2*, WT plants reached this height after ~2 months, whereas mutant plants required 9-10 months. After bark and pith removal, secondary xylem was air-dried, ground to a fine powder, and analyzed at the Laboratory of Chemical Analysis, Tallinn University of Technology (TalTech, Estonia). Structural carbohydrates and lignin were quantified according to the National Renewable Energy Laboratory (NREL) protocol for biomass compositional analysis. Secondary xylem diameters of each sample are shown in Supplementary Table 13.

Computer model definition

Quantitative model construction

A multi-compartmental ordinary differential equation (ODE) model was developed to describe auxin (IAA) subcellular transport, metabolism, and homeostasis in Arabidopsis thaliana root cells. The model incorporates two distinct auxin pools, active (free IAA) and inactive (conjugated IAA), distributed across four compartments: apoplast, cytoplasm, vacuole (active), and vacuole

(inactive). Transport kinetics are parameterized using empirical steady-state protein abundance data from proteomics and transcriptomics and literature reports and unknown rate constants are calibrated to fit experimentally measured active (free IAA) and inactive (vacuole enriched conjugates, IAA-Asp, IAA-Glu) auxin concentrations in wild-type and double *wat* mutant plants.

General model structure

The model comprises four state variables representing quantitative auxin concentrations: A_{cyt} (cytoplasmic active IAA), A_{vac_act} (vacuolar active IAA), A_{vac_inact} (vacuolar inactive IAA), and A_{apo} (apoplastic active IAA). Active IAA moves between the apoplast and cytoplasm via plasma membrane (PM) transporters, and enters the vacuole via tonoplast-localized hypothetical transporters (i.e. ABCB-like transporters). Upon entering the vacuole, IAA is largely conjugated. Inactive IAA pool can either be degraded at the rate k_{deg} or exported back to the cytoplasm by the WAT transporters. GH3-mediated conjugation in the cytoplasm at the rate k_{GH3} also removes active IAA from the system. A constant synthesis term (synth) provides basal auxin production in the system.

The ODE system is defined as changes in fluxes between cell compartments:

$$\frac{dA_{cyt}}{dt} = J_{LAX} - J_{PIN} - J_{ABCB_{PM}} + J_{pass_{PM}} - J_{ABCB_{vac}} + J_{WAT} - J_{pass_{ton}} + synth - J_{GH3}$$

$$\frac{dA_{vac_act}}{dt} = J_{ABCB_{vac}} + J_{pass_{ton}} - J_{inact}$$

$$\frac{dA_{vac_inact}}{dt} = J_{inact} - J_{WAT} - J_{deg}$$

$$\frac{dA_{apo}}{dt} = J_{PIN} - J_{LAX} + J_{ABCB_{PM}} - J_{pass_{PM}}$$

Where transport fluxes follow general Michaelis-Menten kinetics and passive IAAH diffusion is governed by the general chemiosmotic model: $J_{pass} = P_{membrane} \cdot (f_{donor} \cdot C_{donor} - f_{acceptor} \cdot C_{acceptor})$, with $f(pH) = 1/(1 + 10^{(pH - pKa)})$ representing the protonated (membrane-permeable) fraction at each

compartment pH. Metabolic fluxes are first-order: $J_{inact} = k_{inact} \cdot A_{vac_act}$, $J_{GH3} = k_{GH3} \cdot A_{cyt}$, $J_{deg} = k_{deg} \cdot A_{vac_inact}$.

Auxin transporter parameterization

Transporter V_{max} values were parameterized using empirically estimated by steady-state transcript abundance levels derived from single cell transcriptome data. A single global scaling factor (SCALE) converts arbitrary abundance units to effective V_{max} values in $\mu M \cdot s^{-1}$, such that V_{max} = SCALE * [average transcript measurement in cambium]. This approach ensures that the relative expression ratios between transporters are preserved while allowing calibration of the absolute transport capacity to match experimentally observed auxin concentrations. K_m constants for each of transporters were derived from literature reports.

Free rate constants governing inactivation, conjugation, degradation, and synthesis were calibrated using a grid-search optimization to simultaneously match four experimental targets: wild-type active auxin (105.0 nM), wild-type inactive auxin (10.8 nM), wat1 mutant active auxin (8.4 nM), and wat1 mutant inactive auxin (22.0 nM). The optimization minimized the sum of weighted squared relative errors across all four targets.

Key model parameters are summarized in Supplementary Table 14.

Model Calibration Against Experimental Data

The calibrated model reproduces experimental measurements of active and inactive auxin pools in both wild-type (WT) and *wat1* mutant Arabidopsis seedlings. Difference in predicted active and inactive auxin are presented in Supplementary Table 15.

The total fitting error across all four targets was 0.6 (wild-type error = 0.4, wat1 error = 0.3). The model captures the key biological observation: WAT recycling maintains an active auxin pool of ~105 nM in wild type, while loss of WAT causes a 13-fold collapse to ~8 nM, with inactive auxin accumulating approximately 2.0-fold in the vacuole (10.9 increases to 22.2 nM).

Genetic Perturbation Scenarios

Six genetic perturbation scenarios were simulated to evaluate the model's ability to explore transport mutant phenotypes and to predict the effect of untested perturbations. For each scenario, the steady-state concentrations were computed and a time-course simulation was performed starting from 105 nM active IAA in the apoplast (equivalent to the WT total active pool), tracking redistribution over 2 hours (7200 s).

Firstly, the WAT gene knockout (*wat*) causes a dramatic collapse of the active auxin pool with a corresponding increase in vacuolar inactive auxin, confirming the essential role of WAT1-mediated recycling in auxin homeostasis. On the other hand, the loss of PIN alone has minimal effect on cytoplasmic auxin because ABCB1/19 provides redundant PM efflux capacity. AUX1/LAX knockout shows modest reduction in active auxin, as passive diffusion and synthesis partially compensate. Combined loss of both ABCB-mediated PM efflux and tonoplast import (abcb double) eliminates vacuolar auxin storage, shifting auxin to the cytoplasm. GH3 knockout (gh3) increases active auxin by removing a major conjugation sink in the cytosol. Difference in auxin intracellular content are presented in Supplementary Table 16.

Global sensitivity analysis

A variance-based Sobol' global sensitivity analysis [66] was performed to quantify the contribution of each parameter to output variance. N = 1,024 base samples were drawn from uniform distributions over ± one order of magnitude for V_{max}, ± factor of 3 for Km values, and wide ranges for rate constants, yielding 16384 total model evaluations. First-order (S1) and total-order (ST) sensitivity indices were computed using the SALib library (https://salib.readthedocs.io/en/latest/). Four outputs were analyzed: (Y1) WT active auxin pool, (Y2) WT inactive auxin pool, (Y3) WT total auxin pool, and (Y4) the wat1/WT active auxin ratio. ST > 1 values typically arise from strong parameter interactions [67].

The sensitivity analysis reveals three key findings. First, the WT active pool is dominated by the synthesis–conjugation balance (synth ST = 1.00; k_{GH3} ST = 1.41), with GH3-mediated conjugation being the single most influential parameter. Second, the WT inactive pool is almost exclusively controlled by the vacuolar degradation rate (k_{deg} ST = 0.85), with all other parameters contributing negligibly. Third, the severity of the wat1 phenotype (wat1/WT active ratio) depends primarily on WAT1 transport kinetics (K_{m_WAT1} ST = 0.34; V_{max_WAT1} ST = 0.25) and vacuolar degradation (k_{deg} ST = 0.31), consistent with the mechanistic model in which WAT1-mediated recycling and vacuolar degradation compete for the inactive auxin pool. Notably, PM transport parameters have moderate influence on all outputs, suggesting that the vacuolar recycling cycle may be the primary auxin homeostatic route rather than PM transport (Supplementary Fig. 11).

Implementation

The model was implemented in Python 3 using NumPy and SciPy. Steady states were computed using the fsolve algorithm (SciPy optimize) with multiple initial guesses to ensure global convergence. Time-course simulations used the LSODA integrator (SciPy integrate.solve_ivp) with adaptive time-stepping (rtol=1e-9, atol=1e-12). The Sobol' sensitivity analysis used the SALib library [68]. Cell compartment visualizations and animations were generated using Matplotlib. All code and data are available at the accompanying repository.

DATA AVAILABILITY

RNA-seq sequencing FASTQ files and raw count matrices have been deposited in the NCBI Gene Expression Omnibus under accession number GSE328658 (https://www.ncbi.nlm.nih.gov/geo/query/acc.cgi?acc=GSE328658). All scripts required to reproduce the results presented in this manuscript are available on GitHub at

https://github.com/DanielCondeLab/WAT-regulation-of-secondary-growth-and-auxin-homeostasis-in-hybrid-poplar

FUNDING

This work was supported by the "Programa de Atracción de Talento César Nombela de la Comunidad Autónoma de Madrid", 2023 call, with reference 2023-T1/BIO-29308, awarded to D.C.; the CNS2025-165335 grant from the “Ministerio de Ciencia, Innovación y Universidades” of Spain, awarded to D.C.; the PID2024-161778OB-I00 grant from the “Ministerio de Ciencia, Innovación y Universidades” of Spain, awarded to M.P. and D.C.; the Severo Ochoa (SO) Program for Centers of Excellence in R&D from the “Agencia Estatal de Investigación” of Spain, grant CEX2020-000999-S (2022 to 2025) to the CBGP. This work has been funded by Ministerio de Ciencia Innovación y Universidades of Spain (PID2024-155159NB-I00 to KW).

AUTHOR CONTRIBUTIONS

D.C. conceived and supervised this study; J.M., M.R. and D.C. designed the experiments; J.M., M.R. and D.C. performed the experiments and data analysis. A.P.D. performed data validation. K.W. designed, developed, and interpreted the quantitative model. I.A., M.P. and D.C. provided resources and funding for this research. I.A., M.P. and D.C. provided data curation and interpretation; J.M., K.W. and D.C. wrote the original draft; all authors reviewed and edited the manuscript.

REFERENCES

1. Reek, J. E. *et al.* More than mitigation: The role of forests in climate adaptation. *Science* **391**, 669–678 (2026).

2. Zhang, J., Nieminen, K., Serra, J. A. A. & Helariutta, Y. The formation of wood and its control. *Current Opinion in Plant Biology* **17**, 56–63 (2014).
3. Spicer, R. & Groover, A. Evolution of development of vascular cambia and secondary growth. *New Phytologist* **186**, 577–592 (2010).
4. Kumar, M., Campbell, L. & Turner, S. Secondary cell walls: biosynthesis and manipulation. *EXBOTJ* **67**, 515–531 (2016).
5. Gómez-Soto, D. *et al.* Single-nucleus transcriptomics revealed auxin-driven mechanisms of wood plasticity to enhance severe drought tolerance in poplar. *Genome Biol* **26**, 312 (2025).
6. Nilsson, J. *et al.* Dissecting the Molecular Basis of the Regulation of Wood Formation by Auxin in Hybrid Aspen. *The Plant Cell* **20**, 843–855 (2008).
7. Brackmann, K. *et al.* Spatial specificity of auxin responses coordinates wood formation. *Nat Commun* **9**, 875 (2018).
8. Smetana, O. *et al.* High levels of auxin signalling define the stem-cell organizer of the vascular cambium. *Nature* **565**, 485–489 (2019).
9. Mäkilä, R. *et al.* Gibberellins promote polar auxin transport to regulate stem cell fate decisions in cambium. *Nat. Plants* **9**, 631–644 (2023).
10. Bhalerao, R. P. & Fischer, U. Environmental and hormonal control of cambial stem cell dynamics. *EXBOTJ* **68**, 79–87 (2017).
11. Tuominen, H., Puech, L., Fink, S. & Sundberg, B. A Radial Concentration Gradient of Indole-3-Acetic Acid Is Related to Secondary Xylem Development in Hybrid Aspen. *Plant Physiology* **115**, 577–585 (1997).
12. Uggla, C., Moritz, T., Sandberg, G. & Sundberg, B. Auxin as a positional signal in pattern formation in plants. *Proc. Natl. Acad. Sci. U.S.A.* **93**, 9282–9286 (1996).

795 13. Skalický, V. *et al.* Fluorescence-activated multi-organelle mapping of subcellular plant
796 hormone distribution. *The Plant Journal* **116**, 1825–1841 (2023).
797 14. Sun, L. *et al.* PIN-LIKES Coordinate Brassinosteroid Signaling with Nuclear Auxin Input in
798 Arabidopsis thaliana. *Current Biology* **30**, 1579-1588.e6 (2020).
799 15. Johnson, D. *et al.* Polar auxin transport is implicated in vessel differentiation and spatial
800 patterning during secondary growth in *Populus*. *Am J Bot* **105**, 186–196 (2018).
801 16. Ranocha, P. *et al.* Walls are thin 1 (WAT1), an Arabidopsis homolog of Medicago truncatula
802 NODULIN21, is a tonoplast-localized protein required for secondary wall formation in fibers:
803 Tonoplastic WAT1 and secondary wall formation. *The Plant Journal* **63**, 469–483 (2010).
804 17. Ranocha, P. *et al.* Arabidopsis WAT1 is a vacuolar auxin transport facilitator required for
805 auxin homoeostasis. *Nat Commun* **4**, 2625 (2013).
806 18. Yao, X., Nie, J., Bai, R. & Sui, X. Amino Acid Transporters in Plants: Identification and
807 Function. *Plants* **9**, 972 (2020).
808 19. Spicer, R., Tisdale-Orr, T. & Talavera, C. Auxin-Responsive DR5 Promoter Coupled with
809 Transport Assays Suggest Separate but Linked Routes of Auxin Transport during Woody Stem
810 Development in Populus. *PLoS ONE* **8**, e72499 (2013).
811 20. Schmidt, H. W. *et al.* Deep tissue profiling of Populus stem at single nucleus level reveals
812 uncharacterized cell types and cell-specific gene regulatory networks. *Genome Biol* **26**, 258
813 (2025).
814 21. Segami, S., Makino, S., Miyake, A., Asaoka, M. & Maeshima, M. Dynamics of Vacuoles and
815 H+-Pyrophosphatase Visualized by Monomeric Green Fluorescent Protein in *Arabidopsis* :
816 Artifactual Bulbs and Native Intravacuolar Spherical Structures. *The Plant Cell* **26**, 3416–3434
817 (2014).

22. Covington, M. F. & Harmer, S. L. The Circadian Clock Regulates Auxin Signaling and Responses in Arabidopsis. *PLoS Biol* **5**, e222 (2007).
23. Dietrich, L., Zweifel, R. & Kahmen, A. Daily stem diameter variations can predict the canopy water status of mature temperate trees. *Tree Physiology* **38**, 941–952 (2018).
24. Chu, T., Wang, Z., Pe'er, D. & Danko, C. G. Cell type and gene expression deconvolution with BayesPrism enables Bayesian integrative analysis across bulk and single-cell RNA sequencing in oncology. *Nat Cancer* **3**, 505–517 (2022).
25. Kim, S., Held, M. A., Zemelis, S., Wilkerson, C. & Brandizzi, F. CGR 2 and CGR 3 have critical overlapping roles in pectin methylesterification and plant growth in *Arabidopsis thaliana*. *The Plant Journal* **82**, 208–220 (2015).
26. Krupková, E., Immerzeel, P., Pauly, M. & Schmülling, T. The *TUMOROUS SHOOT DEVELOPMENT2* gene of Arabidopsis encoding a putative methyltransferase is required for cell adhesion and co-ordinated plant development. *The Plant Journal* **50**, 735–750 (2007).
27. Paynel, F. *et al.* Kiwi fruit PMEI inhibits PME activity, modulates root elongation and induces pollen tube burst in Arabidopsis thaliana. *Plant Growth Regul* **74**, 285–297 (2014).
28. Matsuura, K. Arabidopsis 3-deoxy-D-manno-oct-2-ulosonate-8-phosphate synthase: cDNA cloning and expression analyses. *Journal of Experimental Botany* **54**, 1785–1787 (2003).
29. Harholt, J. *et al.* ARABINAN DEFICIENT 1 Is a Putative Arabinosyltransferase Involved in Biosynthesis of Pectic Arabinan in Arabidopsis. *Plant Physiology* **140**, 49–58 (2006).
30. Hiroguchi, A., Sakamoto, S., Mitsuda, N. & Miwa, K. Golgi-localized membrane protein AtTMN1/EMP12 functions in the deposition of rhamnogalacturonan II and I for cell growth in Arabidopsis. *Journal of Experimental Botany* **72**, 3611–3629 (2021).
31. Vanholme, R., Demedts, B., Morreel, K., Ralph, J. & Boerjan, W. Lignin Biosynthesis and Structure. *Plant Physiology* **153**, 895–905 (2010).

32. Liao, H.-S., Chung, Y.-H. & Hsieh, M.-H. Glutamate: A multifunctional amino acid in plants. *Plant Science* **318**, 111238 (2022).
33. Schepetilnikov, M. *et al.* GTPase ROP2 binds and promotes activation of target of rapamycin, TOR, in response to auxin. *EMBO J* **36**, 886–903 (2017).
34. Schepetilnikov, M. & Ryabova, L. A. Auxin Signaling in Regulation of Plant Translation Reinitiation. *Front. Plant Sci.* **8**, 1014 (2017).
35. Scarpin, M. R., Leiboff, S. & Brunkard, J. O. Parallel global profiling of plant TOR dynamics reveals a conserved role for LARP1 in translation. *eLife* **9**, e58795 (2020).
36. Ko, D. *et al.* Recruitment of bifunctional regulator thermospermine to methylated ribosomes directs xylem fate. *Science* **391**, 694–699 (2026).
37. Kirui, A. *et al.* A pectin methyltransferase modulates polysaccharide dynamics and interactions in Arabidopsis primary cell walls: Evidence from solid-state NMR. *Carbohydrate Polymers* **270**, 118370 (2021).
38. Conde, D., González-Melendi, P. & Allona, I. Poplar stems show opposite epigenetic patterns during winter dormancy and vegetative growth. *Trees* **27**, 311–320 (2013).
39. Tang, Y. *et al.* Cotton WATs Modulate SA Biosynthesis and Local Lignin Deposition Participating in Plant Resistance Against Verticillium dahliae. *Front. Plant Sci.* **10**, 526 (2019).
40. Lee, J. *et al.* Brassinosteroid-BZR1/2-WAT1 module determines the high level of auxin signalling in vascular cambium during wood formation. *New Phytologist* **230**, 1503–1516 (2021).
41. Novák, O. *et al.* Tissue-specific profiling of the *Arabidopsis thaliana* auxin metabolome. *The Plant Journal* **72**, 523–536 (2012).

42. Ibañez, C. *et al.* Overall Alteration of Circadian Clock Gene Expression in the Chestnut Cold Response. *PLoS ONE* **3**, e3567 (2008).
43. Chen, Y., Chen, L., Lun, A. T. L., Baldoni, P. L. & Smyth, G. K. edgeR v4: powerful differential analysis of sequencing data with expanded functionality and improved support for small counts and larger datasets. *Nucleic Acids Research* **53**, gkaf018 (2025).
44. Benjamini, Y. & Hochberg, Y. Controlling the False Discovery Rate: A Practical and Powerful Approach to Multiple Testing. *Journal of the Royal Statistical Society Series B: Statistical Methodology* **57**, 289–300 (1995).
45. Adrian Alexa, J. R. topGO. Bioconductor https://doi.org/10.18129/B9.BIOC.TOPGO (2017).
46. Berardini, T. Z. *et al.* Functional Annotation of the Arabidopsis Genome Using Controlled Vocabularies. *Plant Physiology* **135**, 745–755 (2004).
47. Zhou, R. *et al.* Haplotype-resolved genome assembly of *Populus tremula* × *P. alba* reveals aspen-specific megabase satellite DNA. *The Plant Journal* **116**, 1003–1017 (2023).
48. Tuskan, G. A. *et al.* The Genome of Black Cottonwood, Populus trichocarpa (Torr. & Gray). *Science* **313**, 1596–1604 (2006).
49. Goodstein, D. M. *et al.* Phytozome: a comparative platform for green plant genomics. *Nucleic Acids Research* **40**, D1178–D1186 (2012).
50. Kanehisa, M., Furumichi, M., Sato, Y., Matsuura, Y. & Ishiguro-Watanabe, M. KEGG: biological systems database as a model of the real world. *Nucleic Acids Research* **53**, D672–D677 (2025).
51. Subramanian, A. *et al.* Gene set enrichment analysis: A knowledge-based approach for interpreting genome-wide expression profiles. *Proc. Natl. Acad. Sci. U.S.A.* **102**, 15545–15550 (2005).

52. Buchfink, B., Reuter, K. & Drost, H.-G. Sensitive protein alignments at tree-of-life scale using DIAMOND. *Nat Methods* **18**, 366–368 (2021).

53. Yu, G., Wang, L.-G., Han, Y. & He, Q.-Y. clusterProfiler: an R Package for Comparing Biological Themes Among Gene Clusters. *OMICS: A Journal of Integrative Biology* **16**, 284–287 (2012).

54. Emms, D. M. & Kelly, S. OrthoFinder: phylogenetic orthology inference for comparative genomics. *Genome Biol* **20**, 238 (2019).

55. Deorowicz, S., Debudaj-Grabysz, A. & Gudyś, A. FAMSA: Fast and accurate multiple sequence alignment of huge protein families. *Sci Rep* **6**, 33964 (2016).

56. Wong, T. K. F. *et al.* IQ-TREE 3: phylogenomic inference software using complex evolutionary models. *Molecular Biology and Evolution* **43**, msag117 (2026).

57. Kalyaanamoorthy, S., Minh, B. Q., Wong, T. K. F., Von Haeseler, A. & Jermiin, L. S. ModelFinder: fast model selection for accurate phylogenetic estimates. *Nat Methods* **14**, 587–589 (2017).

58. Hoang, D. T., Chernomor, O., Von Haeseler, A., Minh, B. Q. & Vinh, L. S. UFBoot2: Improving the Ultrafast Bootstrap Approximation. *Molecular Biology and Evolution* **35**, 518–522 (2018).

59. Letunic, I. & Bork, P. Interactive Tree of Life (iTOL) v6: recent updates to the phylogenetic tree display and annotation tool. *Nucleic Acids Research* **52**, W78–W82 (2024).

60. Engler, C. *et al.* A Golden Gate Modular Cloning Toolbox for Plants. *ACS Synth. Biol.* **3**, 839–843 (2014).

61. Gallardo, F. *et al.* Expression of a conifer glutamine synthetase gene in transgenic poplar. *Planta* **210**, 19–26 (1999).

911 62. Ramos-Sánchez, J. M. *et al.* Real-time monitoring of PtaHMGB activity in poplar
912 transactivation assays. *Plant Methods* **13**, 50 (2017).
913 63. Ribeiro, C. L. *et al.* The uncharacterized gene *EVE* contributes to vessel element dimensions
914 in *Populus*. *Proc Natl Acad Sci USA* **117**, 5059–5066 (2020).
915 64. González-García, M.-P., Bustillo-Avendaño, E., Sanchez-Corrionero, A., Del Pozo, J. C. &
916 Moreno-Risueno, M. A. Fluorescence-Activated Cell Sorting Using the D-Root Device and
917 Optimization for Scarce and/or Non-Accessible Root Cell Populations. *Plants* **9**, 499 (2020).
918 65. Hao, Y. *et al.* Dictionary learning for integrative, multimodal and scalable single-cell analysis.
919 *Nat Biotechnol* **42**, 293–304 (2024).
920 66. Saltelli, A. Making best use of model evaluations to compute sensitivity indices. *Computer*
921 *Physics Communications* **145**, 280–297 (2002).
922 67. Saltelli, A. *et al.* Variance based sensitivity analysis of model output. Design and estimator for
923 the total sensitivity index. *Computer Physics Communications* **181**, 259–270 (2010).
924 68. Herman, J. & Usher, W. SALib: An open-source Python library for Sensitivity Analysis. *JOSS*
925 **2**, 97 (2017).

Supplementary Files

This is a list of supplementary files associated with this preprint. Click to download.

- SupplementaryTables111.xlsx
- SupplementaryFigures110.pdf
- SupplementaryMovie1.mp4
- DocumentS1SuppFigs111SuppTables1216Moviesfiglegend.pdf
- SupplementaryTables111.xlsx
- SupplementaryMovie2.mp4